



Structure and chemical composition of the Mg electrode during cycling in a simple glyme electrolyte

Konstantinos Dimogiannis^{a,†}, Andrzej Sankowski^{a,b,†}, Conrad Holc^{a,d},
Christopher D.J. Parmenter^e, Graham N. Newton^{a,d}, Darren A. Walsh^{a,d}, James O'Shea^c,
Andrei N. Khlobystov^b, Lee R. Johnson^{a,d,*}

^a Nottingham Applied Materials and Interfaces Group, School of Chemistry, University of Nottingham, Nottingham NG7 2TU, United Kingdom

^b School of Chemistry, University Park, University of Nottingham, Nottingham NG7 2RD, United Kingdom

^c School of Physics, University of Nottingham, Nottingham NG7 2RD, United Kingdom

^d The Faraday Institution, Harwell Campus, Didcot OX11 0RA, United Kingdom

^e Nanoscale and Microscale Research Centre, University of Nottingham, Nottingham NG7 2RD, United Kingdom

ARTICLE INFO

Keywords:

Focused-ion beam
Magnesium-ion battery
Mg(TFSI)₂
Tetraglyme
Solid electrolyte interphase

ABSTRACT

The volumetric energy density of magnesium exceeds that of lithium, making magnesium batteries particularly promising for next-generation energy storage. However, electrochemical cycling of magnesium electrodes in common battery electrolytes is coulombically inefficient and significant charging and discharging overpotentials are observed. Several additives and electrolyte formulations based on Mg(TFSI)₂-glyme electrolytes have been proposed as solutions to these problems. However, the impact and value of these advances is often hard to discern due to a lack of knowledge of the composition and performance of the Mg electrode in the underlying Mg(TFSI)₂-glyme electrolyte. In this paper, the chemical and structural changes that occur during electrochemical cycling of Mg in Mg(TFSI)₂-glyme electrolyte solutions are described for the first time. Using focused ion beam-scanning electron microscopy, we show that the Mg deposited during cycling consists of a shell of degradation products, which in turn surrounds an active Mg core. These structures undergo expansion and contraction during cycling due to incorporation of Mg into the core, resulting in structural deformation and degradation of the deposits. Using this structural model, we discuss the complexities observed during electrochemical cycling of Mg electrodes and elucidate the origins of the overpotentials observed during charging. The new understanding and methodology presented here will allow the impact of electrolyte additives on the performance of the Mg electrode to be resolved.

1. Introduction

The Mg battery is potentially a high-energy, sustainable successor to the lithium-ion battery (Li-ion); Mg has a highly negative standard reduction potential (0.6 V vs Li⁺/Li) and a volumetric capacity almost twice that of metallic Li (3833 mAh cm⁻³ vs 2046 mAh cm⁻³), making Mg batteries a particularly attractive prospect for the automotive industry [1–5]. Mg is abundant and less expensive than Li, alleviating some of supply concerns inherent to Li-ion technology [1,4,6]. Moreover, Mg metal is less susceptible to the growth of dendrites during electrochemical cycling than Li metal, mitigating a typical failure mechanism and safety challenge associated with Li batteries [7,8].

Despite these opportunities, two major challenges are hindering development of the Mg battery: (1) intercalation-based positive electrodes for Mg batteries are limited by the low rates of Mg²⁺ insertion and diffusion in the solid state [9]; (2) conventional electrolyte solutions are not simultaneously compatible with Mg negative electrodes and intercalation-based positive electrodes [10–12]. The primary challenge at the negative electrode is the reactivity of metallic Mg, which reacts with most electrolyte solutions upon contact to form a passivating layer which is assumed to be impermeable to Mg²⁺ ions, inhibiting reversible cycling [8,13–16]. A series of innovations in Mg electrolyte development have been reported over the past decades [2,17–32], many of which have increased cycling performance. These developments are

* Corresponding author.

E-mail address: lee.johnson@nottingham.ac.uk (L.R. Johnson).

† These authors contributed equally to this work.

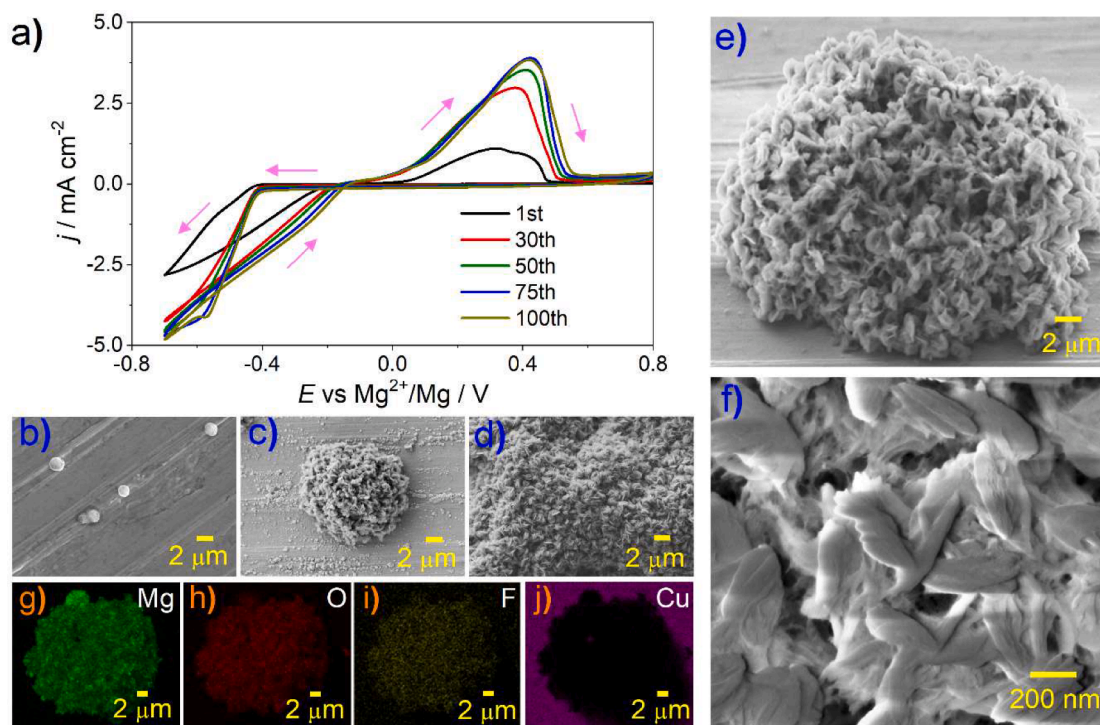


Fig. 1. Cyclic voltammetry and imaging of the Mg electrode after discharge showing the growth of the deposit structure. a) Cycling of a Cu electrode in 0.5 M Mg(TFSI)₂-4 G for 100 cycles. SEM images of the Cu electrodes after b) 1 cycle, c) 30 cycles, and d) 100 cycles showing the growth of the particle. Images (b-e) were acquired using a standard secondary electron detector. Image e) was taken at a stage tilt of 54° and, f) high resolution image of the deposit using in-lens detector. g-j) EDX maps for Mg, O, F, and Cu for a Mg deposit after 30 cycles. Cyclic voltammograms were recorded with Mg reference and counter electrodes, between -0.7 V and 0.8 V vs Mg²⁺/Mg at a scan rate of 100 mV s⁻¹.

often ascribed to the fact that these electrolytes do not passivate the Mg surface. However, such novel electrolyte solutions have not proven sufficiently stable at the positive potentials experienced by high-voltage positive electrodes. More practical systems based on *closo*-borane salts in glyme ethers were developed subsequently, but the synthesis of these systems is complex [33,34].

In recent years, the development of electrolytes for the Mg battery has focussed on the use of electrolytes based on simple salts, such as magnesium(II) bis(trifluoromethanesulfonyl)imide (Mg(TFSI)₂), magnesium tetrakis(hexafluoro-isopropoxy) borate (Mg[B(HFIP)₄]₂), and magnesium fluorinated alkoxyaluminate (Mg[Al(HFIP)₄]₂) dissolved in glyme ethers [15,35–43]. Mg(TFSI)₂-glyme systems are now often used as base electrolytes into which additives are introduced to promote reversible electrochemical cycling of Mg [44,45]. In the absence of additives, it is purported that cycling occurs at a low coulombic efficiency (CE) (<80%) and at large overpotentials, phenomena that are often ascribed to passivation of the Mg surface [8,13–16]. However, it has been shown by us and others that the Mg electrode can be cycled in Mg(TFSI)₂-glyme electrolytes at low overpotentials, even when it is covered with a passivating layer and without the need for electrolyte additives such as Cl⁻ or BH₄⁻ [46–53]. In order to critically assess the impact of additives in future studies it is essential that the true performance and structure of the additive-free standard is determined.

Numerous groups have analysed the surface chemistry and structure of the Mg deposited during cycling in Mg(TFSI)₂-glyme electrolytes [35, 36,46,47,50,53,54,55]. Despite these advances in understanding of the performance and chemistry of the Mg electrode, very little is known about the growth and structure of the deposited Mg metal and, critically, how it affects the electrochemical behaviour of Mg. Understanding the electrochemical cycling of Mg in additive-free Mg(TFSI)₂-glyme electrolytes is a critical first step in understanding the challenges associated with the Mg electrode and is essential if we are to clearly understand the impact of additives on the battery chemistry. The importance of this

understanding is exemplified by analogous research into the Li metal electrode [56], where careful analysis has shown that volume change during plating and stripping of Li results in mechanical instability of the solid electrolyte interphase (SEI) leading to consumption of the electrolyte, accumulation of 'dead' Li, and increased resistance. This understanding has led to the renaissance in the development of Li metal and solid-state batteries [57–62]. Focused ion beam-scanning electron microscopy (FIB-SEM) has proven a promising method of analysing alkali-metal electrodes and their surface structures, and has been used to study dendrite formation at the surface of lithium and to understand the formation of 'dead' Li [56,63]. Without a similar understanding to that developed for the Li electrode, progress in development of Mg electrode will stall.

In this contribution, we describe the use of electrochemical analysis in combination with state-of-the-art FIB-SEM to reveal new insights into the mechanism of electrochemical cycling of Mg electrodes in additive-free Mg(TFSI)₂-glyme electrolyte solutions. Correlation of the electrochemical phenomena with microscopic insights into the dynamic structural changes that occur during cycling reveals that Mg deposits comprising discrete layers of active and inactive Mg form during electrochemical cycling. Moreover, we show how Mg²⁺ ions permeate the deposits, where cycling of active Mg metal occurs with the structures, and how these effects result in structural deformation to accommodate growth of Mg. Finally, we use the insights obtained using these measurements to rationalise the performance of Mg electrodes during use, including their overpotentials and poor coulombic efficiency.

2. Results and discussion

2.1. Chemical and structural analysis of the Mg electrode surface

Mg deposits were formed by cycling a Cu electrode in a Mg(TFSI)₂-tetraglyme (4G) solution between -0.7 and 0.8 V vs Mg²⁺/Mg for 100

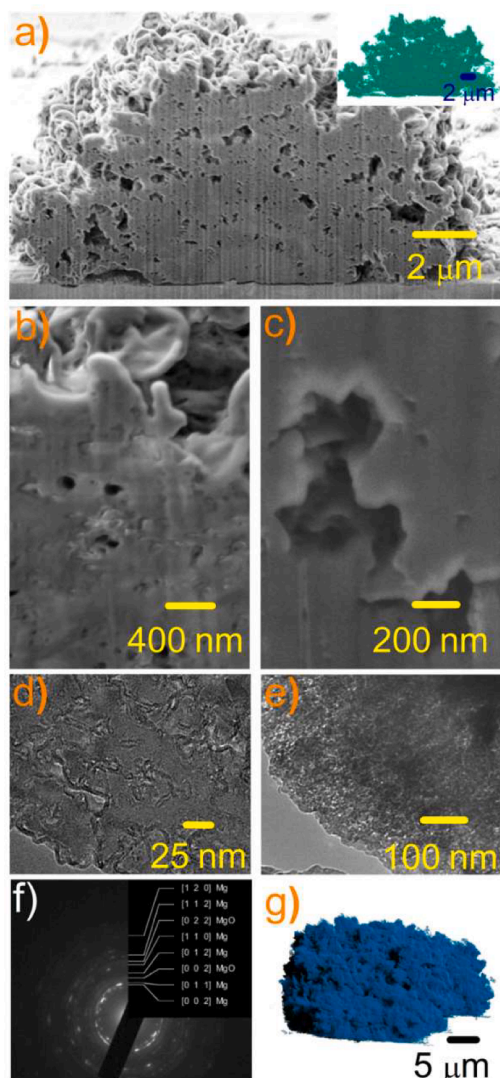


Fig. 2. Chemical and structural 3D analysis of a Mg deposit cross-section after discharge. a-c) Secondary electron images of the exposed cross-section at different magnifications, d-e) TEM images and f) electron-beam diffraction of the Mg deposit. g) Image of a three-dimensional model of the deposit, constructed from SEM images of successive cross-sections and a) inset, an image of a single cross-section from the model showing the pores in white. See Supplementary Note 2 for further discussion of the modelling process. The cycling conditions were as described in Fig. 1a, and cycling was stopped at 0.8 V vs Mg^{2+}/Mg .

cycles (Fig. 1a). The reduction of Mg^{2+} to Mg (charge reaction) began at -0.5 V during the negative-potential sweep and continued to the negative-potential limit. During the subsequent positive sweep, the reduction current was higher positive of ca. -0.55 V than during the prior negative sweep, which is indicative of a nucleation process (discussed below). Oxidation of metallic Mg (discharge reaction) began at -0.05 V and proceeded until about 0.5 V. The peak currents increased as the number of cycles increased (Fig. 1a), a phenomenon known as conditioning and which is due to purification of the electrolyte solution and the formation of an interphase between the metallic Mg and the electrolyte solution [64,53,54]. A similar response was obtained in other glyme ethers, suggesting that a general mechanism operated in these solvents (Figure S1). After 1, 30 and 100 cycles, discharged electrodes were transferred to an SEM chamber and the surface was examined using secondary-electron imaging (Fig. 1b-d). All data described in this work were obtained using a controlled atmosphere, in which exposure of

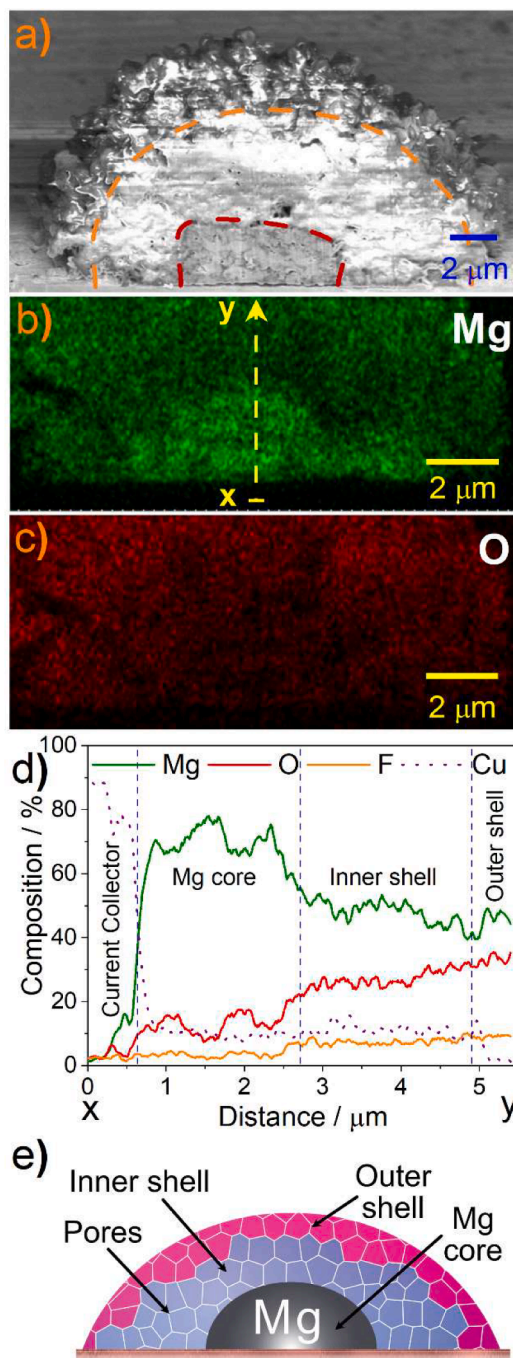


Fig. 3. 3D Analysis of a Mg deposit cross-section demonstrating the presence of a layered structure. a) In-lens secondary electron image highlighting the 3 regions of the particle: Mg-rich inner core, MgO-rich outer core, and the shell. Dashed lines indicate the separate shell structures and the Mg core. EDX mapping showing the elemental distribution of b) Mg, c) O, and d) a line scan of the cross section showing elemental intensity from point x to point y in b), e). Schematic representation of the deposit structure.

the Mg to water and air was avoided. As previously reported, SEM imaging revealed the formation of discrete, dome-shaped deposits (Fig. 1c), which were not removed during the discharge process as would be expected during typical electrochemical cycling of metal electrodes. The SEM images shown in Figure S2 of deposits formed during galvanic cycling at low (0.5 mA cm^{-2} , 4 mAh cm^{-2}) and high (2 mA cm^{-2} , 4 mAh cm^{-2}) current density showed that the morphology is similar when formed by voltammetry and galvanostatic cycling at

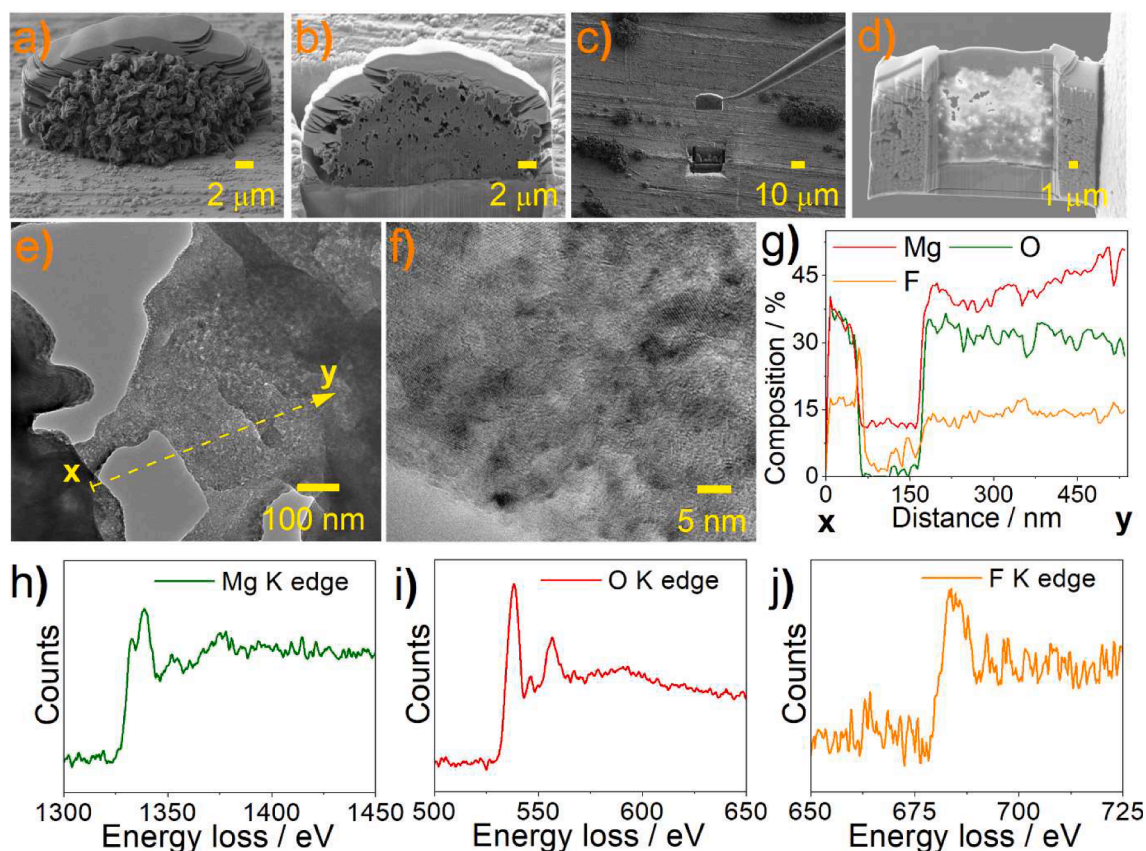


Fig. 4. High resolution TEM analysis of a Mg deposit cross-section showing the internal microstructure. The analysis was performed at a pore boundary in the outer core. a-d) Secondary electron images of the cross-section extraction and lift out process. e,f) TEM images of the cross-section at different magnifications. g) Line scan from point x to y on image e) showing elemental composition. h-j) EELS spectra of Mg, O and F, respectively.

different rates. We previously demonstrated that Mg is stored in these deposits [53]. The mean diameters of the deposits increased from $\sim 1 \mu\text{m}$ after the first cycle to $10\text{--}12 \mu\text{m}$ after 30 cycles and $>20 \mu\text{m}$ after 100 cycles. Intriguingly, the current and electrochemical profile did not change significantly as the size of the Mg deposits increased. The absence of a correlation between the apparent surface area and current indicates that the cycling mechanism is complex and differs from that of classical metal-cycling theory. Understanding this phenomenon requires nanoscale analysis of structural changes occurring during electrochemical cycling of Mg, as well as detailed chemical analysis of the Mg deposits.

High-resolution SEM imaging of the Mg deposits after 30 cycles revealed that they had rough, highly textured surfaces, consisting of plate-like crystallites with dimensions of $200\text{--}700 \text{ nm}$ by $50\text{--}100 \text{ nm}$ that were loosely aggregated with $\sim 100 \text{ nm}$ gaps between the grains (Fig. 1e). Energy dispersive x-ray (EDX) mapping of the electrode surfaces confirmed that the Cu surface between the deposits remained free of Mg (that is, the Mg was localized to the deposits) (Fig. 1g-j and Figure S3). Low magnification images of electrode surfaces after deposition suggest that the Mg preferentially deposited along defect sites (scratches from polishing) in an ordered fashion (Figure S4). Surface characterisation by X-ray photoelectron spectroscopy (XPS) is shown in Figure S5 and its analysis is discussed in Supplementary Note 1. XPS analysis of the electrode surface revealed peaks associated with TFSI⁻ ions (C-F, S=O, O=S=O), which gave way to increased amounts of inorganic Mg salts (Mg-F, Mg-S) after extended cycling. C1s spectra recorded after 30 and 100 cycles revealed the presence of C-O_x, due to the presence of glyme ethers and their degradation products, but we cannot entirely rule out reaction with trace CO₂. This is consistent with the formation of an interphase on the Mg surface that was initially rich

in glyme ethers and TFSI⁻ anions, but then reacted to form a predominantly inorganic interphase consisting of nanocrystalline MgO and small quantities of MgS and MgF₂. Significantly, a small signal appeared at 49 eV due to the presence of metallic Mg, indicating that Mg deposition was occurring close to the topmost layer of the deposit. We note that bulk MgO and MgF₂ are poor conductors of Mg²⁺ ions, suggesting that the process of ion transport into the structure is unlikely to be limited to the solid-state pathway and must proceed via another route [65,66].

2.2. Chemical and structural analysis of the Mg electrode cross-section

The fact that the electrochemical performance of Mg deposits cannot be explained by changes in surface area indicates that much of the charge-discharge chemistry, including changes in the interphase structure and distribution of active Mg, occurs within the deposits. The internal structure of the Mg deposits was studied in the discharged state ($0.8 \text{ V vs Mg}^{2+}/\text{Mg}$) by etching the deposits using a FIB. SEM images of the resulting cross-sections were recorded and typical examples are shown in Fig. 2a-c. The images demonstrate that the core was patterned by a tortuous 3D network of $1\text{--}250 \text{ nm}$ wide pores. A three-dimensional reconstruction of successive cross-sections demonstrates that these pores contributed approximately 14% to the particle volume in the discharged state and permeated the entire structure of the dome-shaped deposit (Figs. 2g and 2a inset), despite the apparent density of the deposit. Development of the 3D models is discussed in Supplementary Note 2, which contains a video showing the cross-sectioning process. Analysis of the internal structure by transmission electron microscopy (TEM) showed that the deposits consisted of aggregated crystallites within a network of tortuous meso-channels (Fig. 2d and 2e). Electron-beam diffraction revealed that the main crystalline phases present were

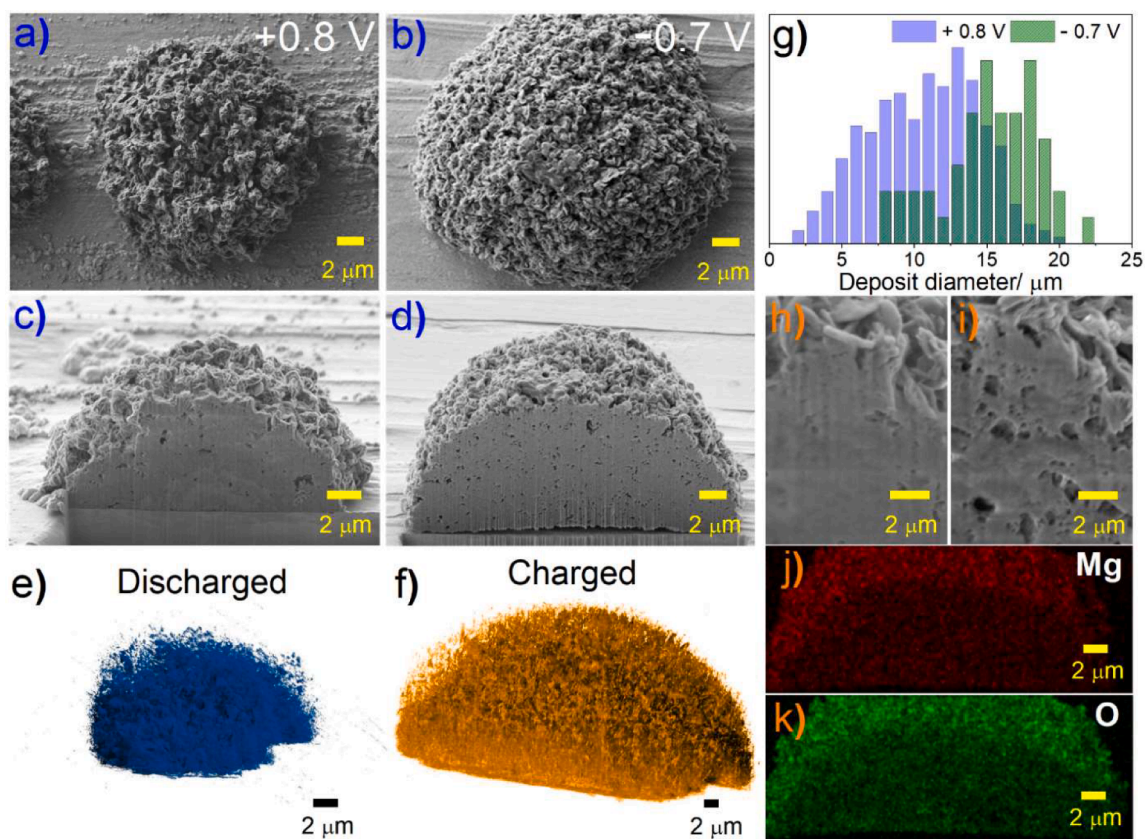


Fig. 5. Cross-sections of a Mg deposit showing the impact of charge and discharge on the structure and chemistry. a,c,e) SEM image, FIB-SEM cross-section and 3D pore structure of a Mg deposit after 30 cycles stopped at 0.8 V vs Mg^{2+}/Mg (discharged state), and b,d,f) when stopped at -0.7 V vs Mg^{2+}/Mg (charged state). g) Histogram showing the deposit size distributions for the charged and discharged deposits. h and i) High magnification SEM images of the interphase of the deposits stopped at 0.8 V and -0.7 V vs Mg^{2+}/Mg respectively. j and k) EDX maps for Mg and O for the cross-section shown in Fig. 5d.

MgO and metallic Mg (Fig. 2f).

To explore the composition of the deposits further, we carried out contrast analysis during electron imaging using an in-lens secondary electron detector (Fig. 3a). These images reveal that the deposits had a complex, onion-like structure consisting of three layers; a ~ 1 μm thick outer shell of aggregated nano-crystallites (an area of mixed dark and bright contrast) surrounding a 5–6 μm thick porous inner shell (a concentric band of brighter contrast), which in turn surrounded a 2–3 μm thick core (an area of dappled grey contrast). The shell chemistry was discussed above, and we define this as the area in which the ratio of Mg to O and F is approximately unity and thus no metallic Mg is present (Fig. 3d). EDX mapping indicates that the inner shell was rich in Mg and O, consistent with a large MgO component but also metallic Mg (Fig. 3b–d). The core was Mg-rich, consistent with metallic Mg. Based on this analysis, we propose that the Mg deposits had the overall structure shown in Fig. 3e, in which a MgO -rich shell surround a Mg-rich core. The entire structure is permeated by micro- and mesopores, which are flooded with electrolyte solution providing channels for Mg^{2+} transport within the electrode resulting in Mg growth within the internal structure, rather than Mg^{2+} crossing the interphase by solid-state diffusion, as would be typically expected.

To obtain a deeper understanding of the pores within the Mg electrode, deposits were coated with Pt, cut to <50 nm slices using the FIB, extracted by a micromanipulator, and transferred under controlled atmosphere for further TEM analysis (Fig. 4a–d). The resulting images revealed a crystalline-aggregate structure, as shown in Figs. 4e and 4f. Electron energy loss spectroscopy (EELS) of the internal pore structure revealed the presence of MgO and MgF_2 (Fig. 4f–h) [67,68]. An EDX line scan across a pore shows that equal amounts of Mg and O were present at the pore surfaces, and the deviation is due to MgF_2 (Fig. 4e). Further into

the structure, the fraction of Mg increases indicating that Mg is plated from the pores. This indicates that an interphase surrounded the internal pores but it should be noted that the images were taken ex situ and that there is a slow reaction between active Mg and the electrolyte solution after deposition (Figure S6). This would account for the interphase seen within the pores.

2.3. Structural fluctuation of the Mg electrode during cycling

The performance of Li electrodes suffers from structural changes in the metal during electrochemical cycling [47–52]. Such processes almost certainly occur during electrochemical cycling of Mg but have not been described thus far. We used focussed ion beam-scanning electron microscopy to study the internal structure the Mg deposit in the charged and discharged states (-0.7 V and 0.8 V vs Mg^{2+}/Mg , respectively) and elucidate the structural changes that accompany charging and discharging of the Mg electrode. Comparison of SEM images show that the average volume of the charged deposit is about 350 % higher than that of the discharged deposit, with mean diameters of ~ 15 and 10 μm for the charged and discharged deposit, respectively (Fig. 5a,b,g). The SEM images also suggest that the porosity of the deposit increases during charging (Fig. 5h,i). This can be clearly seen in 3D models of the pore structure after discharge and charge, which have pore volumes of 62 μm^3 and 456 μm^3 , respectively (Fig. 5e,f). These data show that Mg does not simply fill the free volume available within the deposit when charged, but expands the deposit to accommodate the new volume, increasing the 3D network of pores. EDX imaging shows that the Mg distribution is more uniform after charging (Fig. 5j,k) confirming that Mg growth occurred throughout the deposit. Assuming that the increase in solid volume is attributable to deposition of metallic Mg, 7.08×10^{-6}

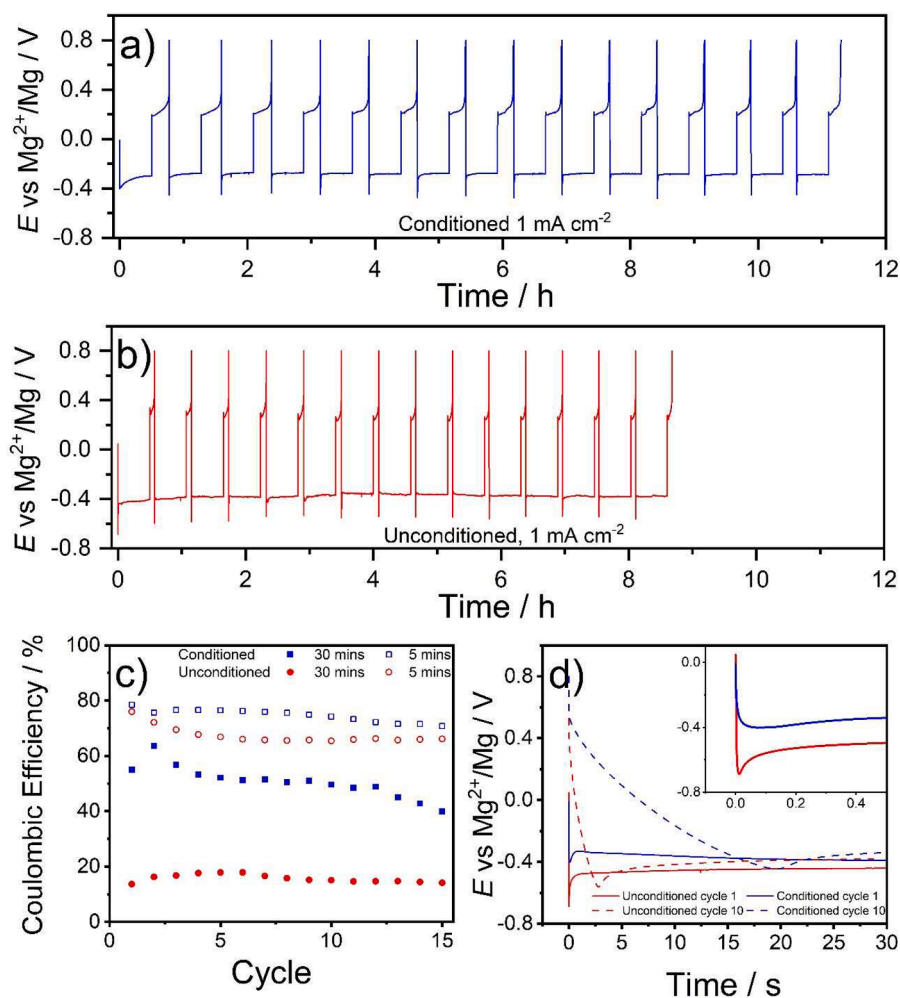
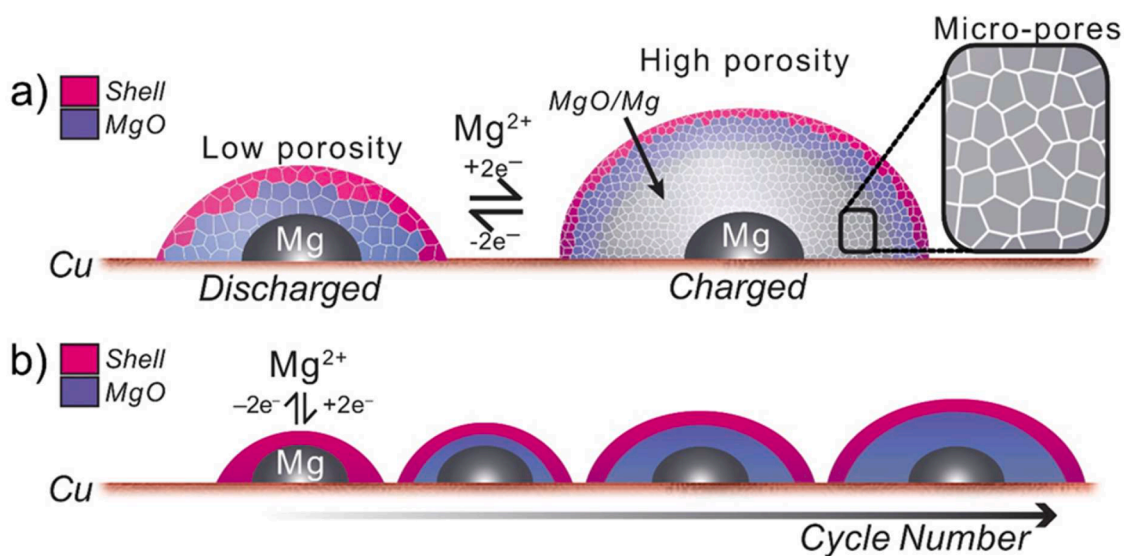


Fig. 6. Cycling profile of the Mg electrode showing the impact of conditioning on the coulombic efficiency and nucleation step. a,b) Galvanostatic cycling profile of the Mg electrode in $Mg(TFSI)_2-4 G$ a) with conditioning and b) without conditioning, charge/discharge rate was 1 mA cm^{-2} , conditioning process is shown in Figure S13. c) Coulombic efficiencies of both systems for different charge/discharge times. d) Galvanostatic cycling highlighting the overpotential needed to drive Mg nucleation at the start of cycling. Cycling was recorded by using a Cu working electrode, and Mg ribbons as both the counter and reference electrodes.



Scheme 1. Schematic of a) the key chemical and structural transformations occurring during cycling of the Mg electrode and b) the growth of the MgO outer core due to accumulation of inactive Mg, as MgO over successive cycles. Expanded region shows the micro and macro pores that permeate the Mg deposit.

mAh of Mg is stored within the deposit, giving a theoretical areal capacity of 4.00 mAh cm^{-2} . Upon discharge, the Mg is removed from the inner shell, the particles shrink and the porosity decreases. These data confirm that the particle fluctuates in size during each cycle to accommodate the deposited Mg. This appears to introduce some mechanical strain as images of cross-sectioned deposits demonstrate delamination of the deposit from Cu current collector (Figure S7 and S8.)

2.4. Mechanism of Mg cycling in practical glyme electrolytes

Schematic 1a summarizes our proposed model for Mg electrode cycling in $\text{Mg}(\text{TFSI})_2$ -glyme electrolyte solutions. On charging (reduction of Mg^{2+} to Mg), Mg^{2+} ions permeate the outer and inner shells through a 3D network of electrolyte filled meso and micro scale pores and plate as Mg on the core, which expands into the inner shell. This process deforms the particle due to the increase in Mg volume, which further increases the porosity. Upon discharge, Mg metal is oxidised and removed from the inner shell until all available Mg has been removed, which is always less than 100 % of that deposited. Formation of the interphase during early cycles limits electrolyte degradation at the surface, but electrolyte solution within the internal channels also undergoes irreversible degradation and limits coulombic efficiency. We suggest this will be exacerbated by volume fluctuation during cycling which would rupture any protective interphases and allow greater electrolyte solution ingress. The degradation process accumulates inactive Mg as MgO in the inner shell, which increases in volume with cycle number (Schematic 1b). The high O to F ratio detected by EDX analysis suggest that even relatively stable ethers will undergo degradation.

Galvanostatic-cycling profiles of Mg at Cu in $\text{Mg}(\text{TFSI})_2$ -4 G for conditioned and unconditioned electrodes at a practical (battery-relevant) current density of 1 mA cm^{-2} (corresponding to 0.5 mAh cm^{-2}) are shown in Fig. 6a,b. The coulombic efficiency was typically 60 % at this current density, and unconditioned electrodes gave lower values. However, if cycling was performed rapidly (5 min charge and discharge), the coulombic efficiency increased to 70–80 %, confirming that the active Mg goes on to react with the electrolyte solution after charging (Fig. 6c). While this value is lower than found with some additives, it is far higher than often reported in the field when considering the impact of additives. This can also be seen during cyclic voltammetry, during which the scan rate had a major impact on coulombic efficiency; at low scan rates (10 mV s^{-1} , long experimental times) most Mg could not be reversibly oxidised (Figure S9) whereas at high scan rates (200 mV s^{-1} , short experimental times) much of the Mg could be oxidised. When galvanostatic cycling was performed with a high areal capacity (4 mAh cm^{-2}) and thus cycle time, the coulombic efficiency was very low, <4 % (Figure S10). This is consistent with a slow degradation reaction between the Mg and the electrolyte solution across the internal pores resulting in the interphase shown in Fig. 4.

The conditioned electrode underwent an overpotential spike of -0.38 V vs Mg^{2+}/Mg at the start of charging, followed by a plateau at -0.29 V vs Mg^{2+}/Mg (Fig. 6d). A similar process was observed for the unconditioned electrode and this effect continued throughout charging (Fig. 6d). The overpotential during cycling has been ascribed to the poor solid-state conductivity of Mg^{2+} in solid interphases and this accounts for the plateau potential [8,13–16]. However the initial overpotential spike occurs at a similar potential regardless of cycle number despite growth of the interphase and its resistance (Fig. 1). To explore this, we partially discharged a Mg electrode such that some Mg remained within the structure (by limiting the upper cut-off voltage to 0.1 V vs Mg^{2+}/Mg) and the overpotential during voltammetry on the subsequent charge decreased to 0.18 V as no nucleation step was needed (Figure S11 and S12). It is also important to note that the plateau overpotential does not increase as the inner shell thickened (as the number of cycles increased), consistent with mass transport through the inner shell predominately occurring in the electrolyte-filled pores (Fig. 6d), rather than in the

solid-state. Following nucleation, charging invariably occurred at an overpotential of 0.3 V , which may be attributable to poor ionic conductivity across the pore interphases, as previously proposed [69]. Importantly, this result suggests that Mg^{2+} reduction and Mg oxidation can proceed at high rates and low overpotentials and that there is no intrinsic electrochemical limitation to moderate rate performance if the challenge of degradation can be overcome (Scheme 1).

3. Conclusion

By combining electrochemical methods with imaging and analysis at the nanoscale by FIB-SEM, TEM, e-beam diffraction and surface spectroscopy, the chemical and structural changes that occur during cycling of the Mg electrode in additive-free $\text{Mg}(\text{TFSI})_2$ -glyme electrolyte solutions have been described in detail for first time. During charging, Mg forms dome-shaped particles with a nanocrystalline surface and porous volume. A cross-sectional analysis revealed a complex internal structure, consisting of a metallic Mg core wrapped in an insulating Mg/MgO inner shell, which was surrounded by an inorganic Mg salt-based (MgS/MgF_2) outer shell. Deposited Mg is incorporated within the MgO inner shell, resulting in a $\sim 400 \%$ expansion in volume and contraction during cycling. The data suggests that even relatively stable ethers undergo degradation resulting in accumulation of inactive Mg as MgO and an ever-increasing electrode volume during cycling. Analysis of the cycling performance shows that both the charge and discharge can occur at an overpotential of just 0.3 V at 1 mA cm^{-2} . The coulombic efficiency depends strongly on the cycling rates and times, demonstrating the importance of studies at various rates to determine the true performance metrics. These data demonstrate the challenges involved in benchmarking the Mg electrode and provide a baseline to which the impact of new additives and salts on the structure and performance of Mg can be compared in future studies.

Declaration of competing interest

The authors declare that they have no known competing financial interests or personal relationships that could have appeared to influence the work reported in this paper.

Acknowledgements

LJ, DW, GN and CH gratefully acknowledge the support of the Faraday Institution's LiSTAR project (EP/S003053/1 FIRG014). ANK thanks the Engineering and Physical Sciences Research Council (EPSRC) for support through MASI project (EP/V000055/1). LJ is grateful to the SUPERGEN energy storage program for support. All authors gratefully acknowledge support from the University of Nottingham's Propulsion Futures Beacon of Excellence for supporting this research. LJ is grateful to the EPSRC fellowship scheme the EPSRC (EP/S001611/1). AS is supported by the Molecular Imaging & Analysis EPSRC Doctoral Thematic Programme. The authors thank the Nanoscale and Microscale Research Centre (nmRC) for providing access to instrumentation and Dr Michael Fay for technical assistance. The work was supported by the Engineering and Physical Sciences Research Council (EPSRC) [under grant EP/S021434/1], [under grant EP/L022494/1] and the University of Nottingham.

Author contributions

K.D., A.S. and C.H. performed the electrochemical and chemical analysis of the electrodes. A.S. and C.D.J. performed the FIB-SEM analysis with supervision from A.N.K.. K.D. and A.S. performed the XPS analysis with supervision from J.O.. G.N.N., D.A.W., A.N.K. and L.R. J supervised the project. All authors wrote the paper.

Data availability

Data analysed during this study are included in the published article and its Supplementary Information. Source data are provided with this paper.

Supplementary materials

Supplementary material associated with this article can be found, in the online version, at doi:10.1016/j.ensm.2024.103280.

References

- [1] D. Larcher, J.M. Tarascon, Towards greener and more sustainable batteries for electrical energy storage, *Nat. Chem.* 7 (2015) 19–29.
- [2] D. Aurbach, et al., Prototype systems for rechargeable magnesium batteries, *Nature* 407 (2000) 724–727.
- [3] Y. Liang, H. Dong, D. Aurbach, Y. Yao, Current status and future directions of multivalent metal-ion batteries, *Nat. Energy* 5 (2020) 646–656.
- [4] M. Fichtner, *Magnesium Batteries: Research and Applications*. RSC Energy and Environment Series vol. 2020, Royal Society of Chemistry, 2019.
- [5] G.N. Newton, L.R. Johnson, D.A. Walsh, B.J. Hwang, H. Han, Sustainability of Battery Technologies: Today and Tomorrow, *ACS Sustain. Chem. Eng.* 9 (2021) 6507–6509.
- [6] A. Ponrouch, et al., Multivalent rechargeable batteries, *Energy Storage Mater* 20 (2019) 253–262.
- [7] D. Li, Y. Yuan, J. Liu, M. Fichtner, F. Pan, A review on current anode materials for rechargeable Mg batteries, *J. Magnes. Alloys* 8 (2020) 963–979.
- [8] R. Attias, M. Salama, B. Hirsch, Y. Goffer, D. Aurbach, Anode-Electrolyte Interfaces in Secondary Magnesium Batteries, *Joule* 3 (2019) 27–52.
- [9] P. Canepa, et al., Odyssey of Multivalent Cathode Materials: Open Questions and Future Challenges, *Chem Rev* 117 (2017) 4287–4341.
- [10] M. Li, et al., Design strategies for nonaqueous multivalent-ion and monovalent-ion battery anodes, *Nat. Rev. Mater.* (2020), <https://doi.org/10.1038/s41578-019-0166-4>.
- [11] E.N. Keyzer, et al., Mg(PF₆)₂-Based Electrolyte Systems: Understanding Electrolyte–Electrode Interactions for the Development of Mg-Ion Batteries, *J. Am. Chem. Soc.* 138 (2016) 8682–8685.
- [12] A. Kopač Lautar, et al., Electrolyte Reactivity in the Double Layer in Mg Batteries: An Interface Potential-Dependent DFT Study, *J. Am. Chem. Soc.* (2020), <https://doi.org/10.1021/jacs.9b12474>.
- [13] J. Muldoon, C.B. Bucur, T. Gregory, Quest for nonaqueous multivalent secondary batteries: Magnesium and beyond, *Chem. Rev.* 114 (2014) 11683–11720.
- [14] R. Mohtadi, F. Mizuno, Magnesium batteries: Current state of the art, issues and future perspectives, *Beilstein J. Nanotechnol.* 5 (2014) 1291–1311.
- [15] Hebié Seydou Hebié, et al., Electrolyte Based on Easily Synthesized, Low Cost Triphenolate– Borohydride Salt for High Performance Mg(TFSI)₂-Glyme Rechargeable Magnesium Batteries, *ACS Appl. Mater. Interfaces* 9 (2017) 28377–28385.
- [16] H. Wang, et al., Advancing Electrolyte Solution Chemistry and Interfacial Electrochemistry of Divalent Metal Batteries, *ChemElectroChem* 8 (2021) 3013–3029.
- [17] T.D. Gregory, R.J. Hoffman, R.C. Winterton, Nonaqueous Electrochemistry of Magnesium: Applications to Energy Storage, *J. Electrochem. Soc.* 137 (1990) 775–780.
- [18] R. Deivanayagam, B.J. Ingram, R. Shahbazian-Yassar, Progress in development of electrolytes for magnesium batteries, *Energy Storage Mater* 21 (2019) 136–153.
- [19] C.J. Barile, E.C. Barile, K.R. Zavadil, R.G. Nuzzo, A.A. Gewirth, Electrolytic Conditioning of a Magnesium Aluminum Chloride Complex for Reversible Magnesium Deposition, *J. Phys. Chem. C* 118 (2014) 27623–27630.
- [20] K.A. See, et al., The Interplay of Al and Mg Speciation in Advanced Mg Battery Electrolyte Solutions, *J Am Chem Soc* 138 (2016) 328–337.
- [21] Ha, J.H. et al. A conditioning-free magnesium chloride complex electrolyte for rechargeable magnesium batteries † *Materials Chemistry A COMMUNICATION*. (2016) 10.1039/c6ta01684g.
- [22] Vardar, G. et al. Mg/O₂ Battery Based on the Magnesium–Aluminum Chloride Complex (MACC) Electrolyte. (2016) 10.1021/acs.chemmater.6b02488.
- [23] R.E. Doe, et al., Novel, electrolyte solutions comprising fully inorganic salts with high anodic stability for rechargeable magnesium batteries † *ChemComm COMMUNICATION*, *Chem Commun* 50 (2014) 243.
- [24] R. Mohtadi, M. Matsui, T.S. Arthur, S.J. Hwang, Magnesium borohydride: from hydrogen storage to magnesium battery, *Angew. Chem. Int. Ed.* 51 (2012) 9780–9783.
- [25] R. Zhang, O. Tutusaus, R. Mohtadi, C. Ling, Magnesium-Sodium Hybrid Battery With High Voltage, Capacity and Cyclability, *Front. Chem* 6 (2018) 611.
- [26] Z. Wang, et al., Degradation of magnesium-ion battery anodes by galvanic replacement reaction in all-phenyl complex electrolyte, *J. Energy Storage* 23 (2019) 195–201.
- [27] A.L. Lipson, et al., Practical Stability Limits of Magnesium Electrolytes, *J. Electrochem. Soc.* 163 (2016) A2253–A2257.
- [28] P. Canepa, et al., Understanding the Initial Stages of Reversible Mg Deposition and Stripping in Inorganic Nonaqueous Electrolytes, *Chem. Mater.* 27 (2015) 3317–3325.
- [29] P. Canepa, et al., Elucidating the structure of the magnesium aluminum chloride complex electrolyte for magnesium-ion batteries, *Energy Env. Sci* 8 (2015) 3718–3730.
- [30] M. Forsyth, L. Porcarelli, X. Wang, N. Goujon, D. Mecerreyes, Innovative Electrolytes Based on Ionic Liquids and Polymers for Next-Generation Solid-State Batteries, *Acc. Chem. Res.* 52 (2019) 686–694.
- [31] H.D. Yoo, et al., Degradation Mechanisms of Magnesium Metal Anodes in Electrolytes Based on (CF₃SO₂)₂N – at High Current Densities, *Langmuir* 33 (2017) 9398–9406.
- [32] C. Liao, et al., The unexpected discovery of the Mg(HMDS)₂/MgCl₂ complex as a magnesium electrolyte for rechargeable magnesium batteries, *J Mater Chem A* 3 (2015) 6082–6087.
- [33] O. Tutusaus, et al., An Efficient Halogen-Free Electrolyte for Use in Rechargeable Magnesium Batteries, *Angew. Chem.* 127 (2015) 8011–8015.
- [34] T.J. Carter, et al., Boron clusters as highly stable magnesium-battery electrolytes, *Angew. Chem. Int. Ed.* 53 (2014) 3173–3177.
- [35] M.S. Ding, T. Diemant, R.J. Behm, S. Passerini, G.A. Giffin, Dendrite Growth in Mg Metal Cells Containing Mg(TFSI)₂ /Glyme Electrolytes, *J. Electrochem. Soc.* 165 (2018) A1983–A1990.
- [36] T. Fukutsuka, et al., New magnesium-ion conductive electrolyte solution based on triglyme for reversible magnesium metal deposition and dissolution at ambient temperature, *Chem. Lett.* 43 (2014) 1788–1790.
- [37] H. Wang, et al., Reversible Electrochemical Interface of Mg Metal and Conventional Electrolyte Enabled by Intermediate Adsorption, *ACS Energy Lett* 5 (2020) 200–206.
- [38] Z. Ma, M. Kar, C. Xiao, M. Forsyth, D.R. MacFarlane, Electrochemical cycling of Mg in Mg[TFSI]₂ /tetraglyme electrolytes, *Electrochem. Commun.* 78 (2017) 29–32.
- [39] Z. Zhao-Karger, et al., Toward Highly Reversible Magnesium-Sulfur Batteries with Efficient and Practical Mg[B(hfp)]₄2 Electrolyte, *ACS Energy Lett* 3 (2018) 2005–2013.
- [40] B. Dlugatch, et al., Evaluation of Mg[B(HFIP)]₄2-Based Electrolyte Solutions for Rechargeable Mg Batteries, *ACS Appl. Mater. Interfaces* (2021), <https://doi.org/10.1021/acsami.1c13419>.
- [41] P. Jankowski, et al., Development of Magnesium Borate Electrolytes: Explaining the Success of Mg[B(hfp)]₄2 Salt, *Energy Storage Mater* (2021), <https://doi.org/10.1016/j.ensm.2021.11.012>.
- [42] T. Pavčnik, et al., On the Practical Applications of the Magnesium Fluorinated Alkoxyaluminate Electrolyte in Mg Battery Cells, *ACS Appl. Mater. Interfaces* 14 (2022) 26766–26774.
- [43] K. Tang, et al., A Stable Solid Electrolyte Interphase for Magnesium Metal Anode Evolved from a Bulky Anion Lithium Salt, *Adv. Mater.* 32 (2020) 1904987.
- [44] J. Wang, et al., Electrostatic Shielding Guides Lateral Deposition for Stable Interphase toward Reversible Magnesium Metal Anodes, *ACS Appl. Mater. Interfaces* 12 (2020) 19601–19606.
- [45] Y. Sun, F. Ai, Y. Lu, Electrolyte and Interphase Design for Magnesium Anode: Major Challenges and Perspectives, *Small* (2022) 2200009, <https://doi.org/10.1002/smll.202200009>.
- [46] N. Sa, et al., Concentration dependent electrochemical properties and structural analysis of a simple magnesium electrolyte: magnesium bis(trifluoromethane sulfonyl)imide in diglyme, *RSC Adv* 6 (2016) 113663–113670.
- [47] S.Y. Ha, et al., Magnesium(II) bis(trifluoromethane sulfonyl) imide-based electrolytes with wide electrochemical windows for rechargeable magnesium batteries, *ACS Appl. Mater. Interfaces* 6 (2014) 4063–4073.
- [48] N.N. Rajput, T.J. Seguin, B.M. Wood, X. Qu, K.A. Persson, Elucidating Solvation Structures for Rational Design of Multivalent Electrolytes—A Review, *Top. Curr. Chem.* 376 (2018) 1–46.
- [49] S. Terada, et al., Thermal and electrochemical stability of tetraglyme-magnesium bis(trifluoromethanesulfonyl)amide complex: Electric field effect of divalent cation on solvate stability, *J. Phys. Chem. C* 120 (2016) 1353–1365.
- [50] R. Jay, et al., Comparative Study of Mg(CB11H12)₂ and Mg(TFSI)₂ at the Magnesium/Electrolyte Interface, *ACS Appl. Mater. Interfaces* 11 (2019) 11414–11420.
- [51] T.J. Seguin, N.T. Hahn, K.R. Zavadil, K.A. Persson, Elucidating non-aqueous solvent stability and associated decomposition mechanisms for mg energy storage applications from first-principles, *Front. Chem.* 7 (2019) 1–13.
- [52] S. Fan, et al., A Simple Halogen-Free Magnesium Electrolyte for Reversible Magnesium Deposition through Cosolvent Assistance, *ACS Appl. Mater. Interfaces* 12 (2020) 10252–10260.
- [53] C. Holc, K. Dimogiannis, E. Hopkinson, L.R. Johnson, Critical Role of the Interphase at Magnesium Electrodes in Chloride-Free, Simple Salt Electrolytes, *ACS Appl. Mater. Interfaces* 13 (2021) 29708–29713.
- [54] I. Shterenberg, et al., Evaluation of (CF₃SO₂)₂N – (TFSI) Based Electrolyte Solutions for Mg Batteries, *J. Electrochem. Soc.* 162 (2015) A7118–A7128.
- [55] J.G. Connell, et al., Tuning the Reversibility of Mg Anodes via Controlled Surface Passivation by H₂O/Cl – in Organic Electrolytes, *Chem. Mater.* 28 (2016) 8268–8277.
- [56] M.J. Zachman, Z. Tu, S. Choudhury, L.A. Archer, L.F. Kourkoutis, Cryo-STEM mapping of solid–liquid interfaces and dendrites in lithium–metal batteries, *Nature* 560 (2018) 345–349.
- [57] Issues and challenges facing rechargeable lithium batteries | *Nature*. <https://www.nature.com/articles/35104644>.
- [58] J. Xiao, et al., Understanding and applying coulombic efficiency in lithium metal batteries, *Nat. Energy* 5 (2020) 561–568.

- [59] J.W. Choi, D. Aurbach, Promise and reality of post-lithium-ion batteries with high energy densities, *Nat. Rev. Mater.* 1 (2016) 16013.
- [60] B. Thirumalraj, et al., Nucleation and Growth Mechanism of Lithium Metal Electroplating, *J. Am. Chem. Soc.* 141 (2019) 18612–18623.
- [61] B. Liu, J.G. Zhang, W. Xu, Advancing Lithium Metal Batteries, *Joule* 2 (2018) 833–845.
- [62] Yu, Z. et al. Molecular design for electrolyte solvents enabling energy-dense and long-cycling lithium metal batteries. *Nat. Energy* 10.1038/s41560-020-0634-5.
- [63] C. Fang, et al., Quantifying inactive lithium in lithium metal batteries, *Nature* 572 (2019) 511–515.
- [64] G. Bieker, et al., The Power of Stoichiometry: Conditioning and Speciation of MgCl₂/AlCl₃ in Tetraethylene Glycol Dimethyl Ether-Based Electrolytes, *ACS Appl. Mater. Interfaces* 11 (2019) 24057–24066.
- [65] B. Li, et al., Kinetic surface control for improved magnesium-electrolyte interfaces for magnesium ion batteries, *Energy Storage Mater* 22 (2019) 96–104.
- [66] J.G. Smith, J. Naruse, H. Hiramatsu, D.J. Siegel, Intrinsic Conductivity in Magnesium-Oxygen Battery Discharge Products: MgO and MgO₂, *Chem. Mater.* 29 (2017) 3152–3163.
- [67] L.P. Zenser, R. Gruehn, B.H. Liebscher, Decomposition of MgF₂ in the Transmission Electron Microscope, *J. Solid State Chem.* 157 (2001) 30–39.
- [68] F. Frati, M.O.J.Y. Hunault, F.M.F de Groot, Oxygen K-edge X-ray Absorption Spectra, *Chem. Rev.* 120 (2020) 4056–4110.
- [69] K. Xu, Electrolytes and interphases in Li-ion batteries and beyond, *Chem. Rev.* 114 (2014) 11503–11618.